www.acsnano.org

Magnetotransport in Graphene/Pb_{0.24}Sn_{0.76}Te Heterostructures: Finding a Way to Avoid Catastrophe

Gregory M. Stephen,* Ivan Naumov, Nicholas A. Blumenschein, Y.-J. Leo Sun, Jennifer E. DeMell, Sharmila N. Shirodkar, Pratibha Dev, Patrick J. Taylor, Jeremy T. Robinson, Paul M. Campbell, Aubrey T. Hanbicki, and Adam L. Friedman*



Downloaded via HARVARD UNIV on December 5, 2022 at 13:52:31 (UTC). See https://pubs.acs.org/sharingguidelines for options on how to legitimately share published articles.

Cite This: ACS Nano 2022, 16, 19346-19353



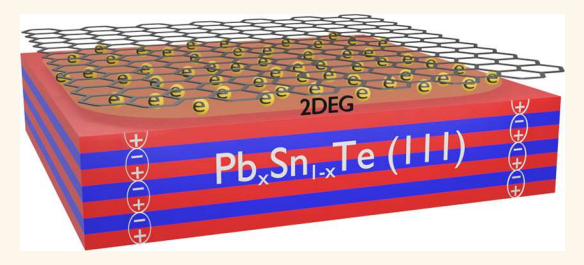
ACCESS I

III Metrics & More

Article Recommendations

Supporting Information

ABSTRACT: While heterostructures are ubiquitous tools enabling new physics and device functionalities, the palette of available materials has never been richer. Combinations of two emerging material classes, two-dimensional materials and topological materials, are particularly promising because of the wide range of possible permutations that are easily accessible. Individually, both graphene and Pb_{1-x}Sn_xTe (PST) are widely investigated for spintronic applications because graphene's high carrier mobility and PST's topologically protected surface states are attractive platforms for spin transport. Here, we combine monolayer



graphene with PST and demonstrate a hybrid system with properties enhanced relative to the constituent parts. Using magnetotransport measurements, we find carrier mobilities up to 20 000 cm²/(V s) and a magnetoresistance approaching 100%, greater than either material prior to stacking. We also establish that there are two distinct transport channels and determine a lower bound on the spin relaxation time of 4.5 ps. The results can be explained using the polar catastrophe model, whereby a high mobility interface state results from a reconfiguration of charge due to a polar/nonpolar interface interaction. Our results suggest that proximity induced interface states with hybrid properties can be added to the still growing list of behaviors in these materials.

KEYWORDS: topological insulators, magnetoresistance, graphene, polar catastrophe, heterostructure, two-dimensional electron gas

eterostructures can have novel properties that are useful for applications or solutions to a variety of physics and engineering problems. Examples include high-mobility two-dimensional electron gases (2DEGs) at the interface between complex oxides caused by charge redistribution to avoid the polar catastrophe, 1-4 the development of blue LEDs in InGaN quantum wells,5 and the fractional quantum Hall effect observed in two-dimensional (2D) electron systems, the latter two of which resulted in Nobel prizes. In heterostructures such as these, hybridization and proximity effects often dominate interactions yielding unforeseen and extraordinary results. Until recently, creating such heterostructures required careful, spotlessly clean growth and interfaces through molecular beam epitaxy (MBE) or other methods. These techniques rely on understanding free energies of formation and are compatible only with carefully paired materials. However, with 2D van der Waals materials like graphene⁸ and topological materials,⁹ these legacy rules no longer apply. Exfoliatable 2D materials can be positioned and stamped arbitrarily on any substrate. Meanwhile, topological

materials have spin—orbit coupling (SOC) that is strong enough to create topologically protected and robust surface states that allow for proximity interactions even without pristine interfaces.¹⁰

Future computing devices provide the most compelling motivation for devising new heterostructures. As current computing technologies approach the inevitable physical and energetic limitations imposed by complementary metal-oxide-semiconductor (CMOS)-based devices, new approaches to memory and logic implementation are paramount. Alternate state variables such as the electron spin and quantum phase are gaining traction as avenues for memory and logic applications. Let's difficult to find individual materials with all the

Received: September 6, 2022 Accepted: October 17, 2022 Published: October 19, 2022





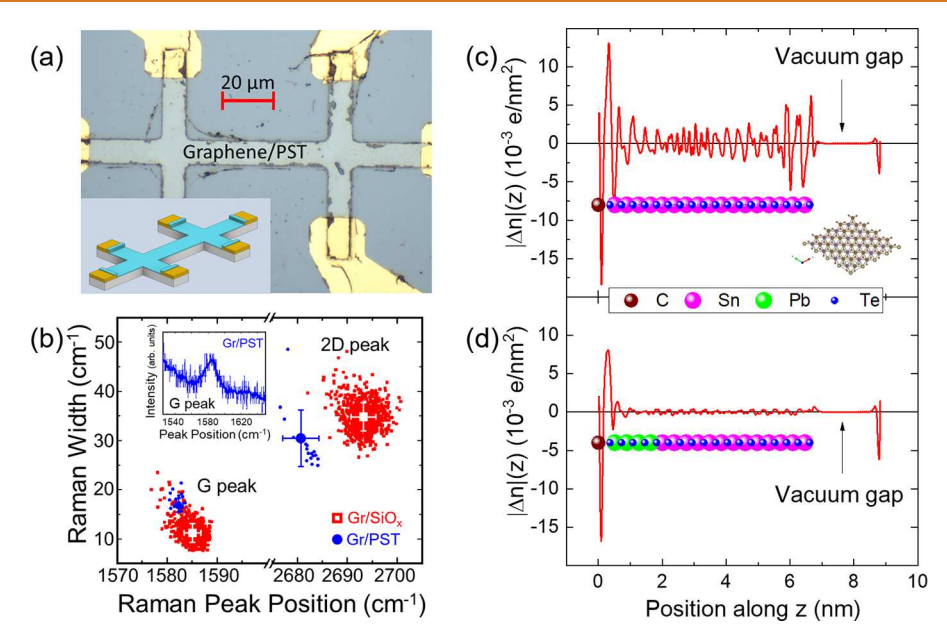


Figure 1. (a) Optical image of the Gr/PST Hall bar. Inset is a schematic of the heterostructure. (b) Graphene G and 2D Raman peak positions vs widths for Gr/SiOx (red squares) and Gr/PST (blue circles). The small symbols are data taken over an extended region of the sample, and the large data point is the average of these points. The error bars represent the mean of the averaged data. The inset is a Raman spectrum around the G peak for the Gr/PST sample. For a strained sample, the G peak should exhibit a splitting.²³ (c, d) Change in planar charge density with the addition of graphene on (c) SnTe and (d) SnTe with the top four layers of Sn replaced by Pb. The circles represent the position of each atom in the supercell. The monolayer graphene induces a charge density wave in the SnTe stack, and the addition of Pb layers drastically attenuates the effect of the graphene.

properties necessary for alternative state variable computing applications. However, we can design composite systems with the required properties by combining materials into heterostructures. For example, because spin diffusion and relaxation are directly related to the carrier mobility, high-mobility materials such as graphene are obvious candidates for useful spintronic devices. 15,16 While graphene has the long spin diffusion length and relaxation times necessary for spin transport, it lacks the SOC needed to manipulate spin through, e.g., external gating that exploits the Rashba effect.¹⁷ On the other hand, topological insulators (TIs) possess the SOC essential for controlling spin transport as well as topologically protected surface states that reduce the influence of surface defects. Indeed, previous research shows that graphene/TI heterostructures exhibit proximity-induced SOC effects using BiSe-based TIs. 10,18 However, TIs are often heavily doped away from the Dirac point. This introduces significant bulk conduction, leading to mobilities that seldom exceed 1000 cm²/(V s). ^{19,20} Combining graphene and topological materials could yield a heterostructure that exhibits the protected, spinpolarized states of the TI with the high mobility of graphene.

Along this line, we fabricate heterostructures of the topological crystalline insulator (TCI) Pb_{0.24}Sn_{0.76}Te (PST) and graphene (Gr) and find evidence of a high-mobility 2D interface conduction state. See the Supporting Information for detailed methods. The strong interaction between the component materials leads to enhanced properties such as a mobility and magnetoresistance greater than the constituent materials. We attribute these enhancements to conduction through a 2DEG formed at the interface. Density functional theory (DFT) analysis reveals that the 2DEG does not inherit the topological character of the PST, which is actually broken by adding graphene to the surface. Rather, the 2DEG arises from a charge redistribution at the interface to avoid the polar

catastrophe at the surface, similar to the widely studied 2DEG in $LaAlO_3/SrTiO_3$. In addition to electrical characterization, in this work, we characterize this hybrid system with both high and low field magnetotransport measurements and estimate spin-based properties, such as lifetimes based on both Shubnikov-de Haas and localization effects. Engineered quantum materials such as this could provide a platform for next-generation spintronic devices.

RESULTS AND DISCUSSION

Figure 1a is an optical image of a measured Hall bar device with a schematic of the heterostructure in the inset. Figure 1b shows the Raman G and 2D peak positions vs widths for Gr/ PST (blue circles) as well as a witness Gr/SiO_x (red squares) sample with graphene prepared in the same way for both samples. In this figure, the small symbols are data taken at multiple locations over extended regions of the samples, and the large symbols represent averages of these data points with the error bars representative of the statistical mean of the data. For the Gr/PST, both the G and 2D peaks shift to lower energy and the G broadens. This is indicative of a reduction of carriers in the graphene²² and is consistent with carriers transferring to a surface state between the graphene and PST. Additionally, there is no evidence of strain in the Gr/PST system that could affect the band structure. Strain manifests as a splitting of the G peak as well as a correlation of the 2D and G peak positions.²³ We do not observe any splitting of the G peak (Figure 1b, inset), and a fit to the 2D peak position vs G peak position is not consistent with strain (see Figure S1b).

This notion of a combined system is supported by DFT calculations of the charge distribution. We consider two extreme cases: (i) a heterostructure of graphene on the purely topological SnTe and (ii) a similar heterostructure with the top four layers of Sn replaced with Pb; the latter case is equivalent

to having four layers of the trivial insulator PbTe on top of the TCI SnTe and is roughly equal to the stoichiometry of our PST film (see Figure S2). This represents a fully phase-segregated alloy of $Pb_{0.24}Sn_{0.76}Se$ where the TCI phase is completely broken at the interface by trivial PbTe. Figure 1c,d shows changes in the electron distribution for graphene on (c) SnTe and (d) 4L-PbSnTe along with the position of each atomic species. Adding graphene breaks band inversion, creating the charge redistribution observed in Figure 1c. When enough Pb is added, the SnTe band inversion is broken and there is no resulting charge density wave created by the graphene, Figure 1d.

While the broken band inversion destroys the topological surface states, an alternate surface state is created by the PST surface. SnTe is a mirror TCI with a mirror Chern number $(C_{+i}C_{-i})/2 = 2.^{24}$ Since the total Chern number $(C_{+i} + C_{-i})$ is zero, the Wannier functions in this system can be chosen to be maximally localized in all three dimensions. Therefore, the electrical polarization, which is expressed in terms of the Berry phase, is a well-defined quantity.²⁵ The calculated total (electronic plus ionic) Berry phase along the [111] direction in the SnTe system is π , indicating that the two (top and bottom) (111) surfaces are polar.^{2,3,26} These surfaces remain polar even if some of the Sn ions are replaced with Pb ions. For the polar surface to be electrostatically stable, it must have a finite external compensating charge density, $\sigma_{
m ext}$ such that $\sigma_{
m ext}$ + $\mathbf{P} \cdot \mathbf{n} = 0$, where \mathbf{P} is the bulk polarization proportional to the total Berry phase.² In the case of the SnTe slabs with Te termination on both sides, the structure has inversion symmetry, although it has a broken bulk stoichiometry. For such a Te-terminated slab, $\sigma_{\rm ext}$ comes from the partial filling of the surface states that fall out of the bulk valence band. Because of the presence of two surfaces related by an inversion center, these surface states localized on the opposite surfaces are doubly degenerate. In principle, they can be removed from the energy window around the Fermi level by passivation (for example, with H atoms) of both surfaces. However, when one of the two (111) Te-terminated surfaces is in contact with graphene, the corresponding surface states (from the graphene side) survive, although they are modified. Our DFT analysis demonstrates that the metallic surface states under the graphene layer are not confined to the very top layer but extend into the bulk region over ~10 layers (see Figures S3 and S4). Thus, a 2DEG is created, similar to that of the $LaAlO_3/SrTiO_3$ interface.^{2,3} This 2DEG appears in both Figure 1c,d, indicating that it is not a direct result of the topological state. Rather, bringing graphene into contact with a PST film not only modifies the surface states associated with $\sigma_{\rm ext}$ but also leads to the redistribution of the electron density across the entire slab.

To understand the electronic properties of this heterostructure, we measured the magnetotransport of graphene, PST, and the Gr/PST heterostructure using standard Hall bar devices. To begin, sheet resistances are 36 k Ω/\Box for the PST and 4.2 k Ω/\Box for the graphene, whereas the heterostructure has a sheet resistance of 3 k Ω/\Box . This suggests conduction is not just a result of parallel conduction channels, which yield a sheet resistance of 3.76 k Ω/\Box . The Hall mobility at 10 K for our bare PST film is 200 cm²/(V s) and for our CVD graphene is 3800 cm²/(V s). However, the heterostructure mobility is measured to be as high as 20 000 cm²/(V s). The quality of the substrate affects the mobility of graphene with atomically smooth hexagonal boron nitride (hBN) being a common

method of improving device quality.²⁷ However, the physics that allows for increased mobility on hBN (atomically smooth, uniform insulator) do not apply to the doped PST film used here. The sheet carrier densities for the graphene and Gr/PST are within a factor of 2 (graphene = 4×10^{12} cm⁻²; PST = 8×10^{12} cm⁻²), suggesting that carrier doping is insufficient to account for the drastic change in mobility. As discussed above, a more likely explanation is a highly conductive channel created through the avoidance of the polar catastrophe. As shown, the interaction between the two materials affects the charge density throughout the entire sample through electronic relaxation, not just at the surface or interface, although the conductive channel is formed at the surface due to the accumulation of charge in that region.

Magnetoresistance (MR) measurements reveal further insight into the character of the conduction in the surface channel. The high-field MR of graphene (red), PST (black), and Gr/PST (blue) at T=300 mK is shown in Figure 2a. The

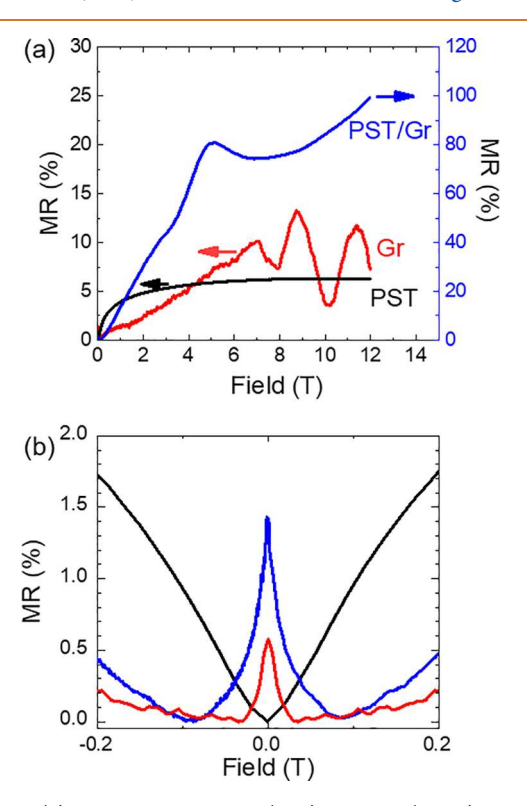


Figure 2. (a) Magnetoresistance (MR) of PST (black), graphene (red), and the Gr/PST heterostructure (blue). SdH oscillations do not appear in the PST but begin around 7 T in graphene and 2 T in the heterostructure. This is explained in part by the large difference in carrier mobilities between the three samples. Only positive field data is shown to emphasize the oscillations. Features are symmetric in the field (see Figures S6 and S7). (b) A magnified view of the low-field region showing the weak localization (WL) peak in the Gr/PST and graphene as well as the lack thereof in PST.

heterostructure shows drastically different behavior compared to the constituent materials. We first note that the PST MR (black line) saturates at 6% with no evidence of Shubnikov-de Haas (SdH) oscillations, while the graphene shows linear MR with sinusoidal oscillations starting around 7 T and a similar overall magnitude as the bare PST. The heterostructure exhibits a combination of the two behaviors but with drastically

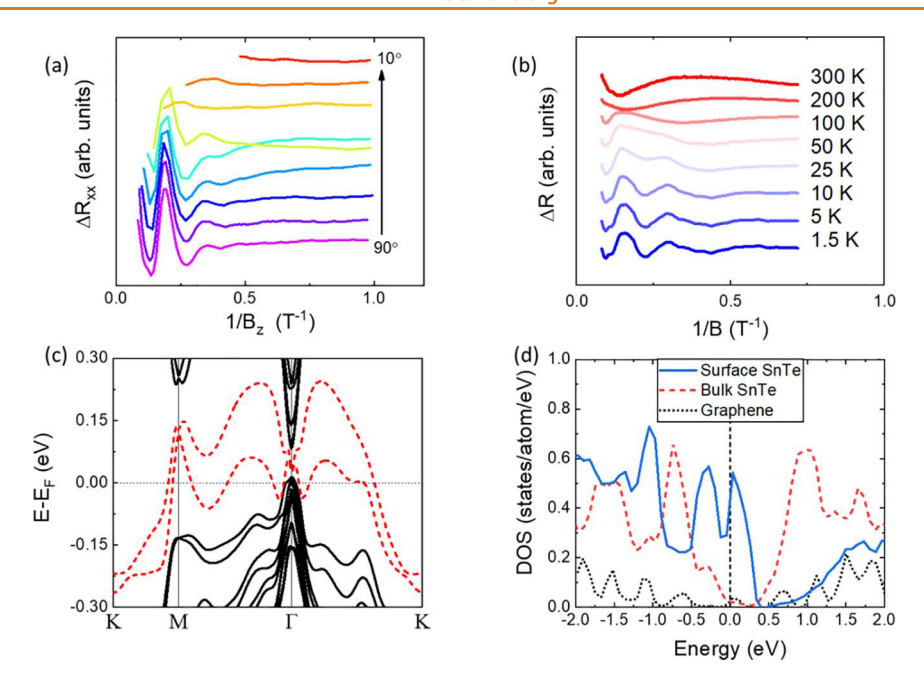


Figure 3. (a) Background subtracted longitudinal resistance measurement, ΔR_{xx} , as a function of $1/B\sin\theta = 1/B_z$ in Gr/PST for various angles at 300 mK. The SdH peak positions are constant as a function of $1/B_z$, indicating we are probing a purely 2D state. (b) Background subtracted longitudinal resistance measurement, ΔR_{xx} , as a function of 1/B in Gr/PST for various temperatures at a 90° angle (out-of-plane field). The peak positions remain constant in temperature but with decreasing amplitude. Fitting of the field dependence at 1.5 K results in a momentum scattering time of 46 fs with temperature dependent fitting yielding an effective mass of $0.0095m_e$. These are $50\times$ and $5\times$ larger than the values for graphene, 1.4 fs and $0.002m_e$, respectively. (c) Calculated band structures for Gr/SnTe. Dashed lines represent the bands corresponding to the surface 2DEG. (d) Partial density of states (DOS) for the graphene (dotted black) as well as the SnTe surface (solid blue) and bulk (dashed red). The majority of available states at the Fermi level come from the surface.

higher MR approaching 100%. The MR is nearly linear up to 2 T, at which point low-frequency SdH oscillations begin. The background at higher fields appears to be sublinear, similar to the PST-only sample. The linear behavior at lower fields could be an indication of topological features as seen in $Bi_2Te_xSe_{1-x}$ topological insulators. Quantum effects like SdH oscillations tend to appear when the quantity $\omega_c \tau > 1$, where ω_c is the cyclotron frequency and τ is a characteristic scattering time. Using the Drude transport model, this can be written as $\mu B >$ 1, where μ is the carrier mobility and B is the applied field.³⁰ In other words, oscillations occur when the carriers complete, or nearly complete, cyclotron orbits between momentum scattering events. Thus, the SdH oscillations, or lack thereof, in each sample are well described by the Hall mobility of each sample. Again, the Hall mobility at 10 K for our bare PST film is 200 cm²/(V s), compared to 3800 cm²/(V s) for the graphene and as high as 20 000 cm²/(V s) for the heterostructure. From the Drude model, this results in the expected onset of SdH oscillations at fields of approximately 0.5 and 7 T for Gr/PST and graphene, respectively, and 50 T for bare PST. This is consistent with the data where oscillations begin in the heterostructure at about 2 T and in graphene at around 7 T and are not observed in the PST. Quantum mobility can also be extracted directly from the SdH oscillations. The quantum mobility is related to the slope of Landau level position vs number and yields $970 \text{ cm}^2/(\text{V s})$ for the graphene and 8040 cm²/(V s) for the heterostructure, consistent with the low-field Hall mobilities.

Figure 2 shows the magnetoresistance for both high and low magnetic fields, demonstrating SdH oscillations in Figure 2a and weak localization in Figure 2b. At higher fields, SdH oscillations appear on top of the MR signal. These oscillations

result from field splitting of the Landau levels and are governed by the momentum scattering in the system. To isolate the oscillatory component, we subtract a background signal from each longitudinal resistance measurement (see Figure S3). Figure 3a shows the results of this background subtraction, ΔR_{xx} , as a function of $1/B_z = 1/B\sin\theta$ for angles from 10° to 90° . The angle corresponds to orientation of the B field with respect to the plane of the PST film. Note the peak positions are constant as a function of $1/B_z$. This indicates coupling only to the z-component of the magnetic field and implies conduction is confined to a 2D state, again consistent with a graphene/PST interface state.

Figure 3b shows the background-subtracted data at temperatures from 1.5 K up to 300 K. The temperature dependence of the SdH amplitude, A, is directly related to the effective carrier mass, m^* . This temperature dependence at field B_r is described by 31

$$A \propto \lambda T / \sin h \, \lambda T \tag{1}$$

where $\lambda = 2\pi^2 k_{\rm B} m^*/\hbar e B_{\rm r}$. Fits of our data yield an effective mass of $m^* = 0.0095 m_{\rm e}$, similar to effective masses previously reported in graphene/WS₂ stacks (see Figure S8).³² When applied to the oscillations in our graphene sample, we see an effective mass of $m^* = 0.002 m_{\rm e}$. A 5× increase in effective mass in the heterostructure seems at odds with the increased Hall mobility in the heterostructure.

This discrepancy in effective mass can be reconciled by examining the scattering time. At a fixed temperature, the decay of the oscillations with 1/B is related to the momentum scattering time $\tau_q = \tau_{\text{SdH}}$ according to 31

$$\ln\left(AB \sinh \frac{2\pi k_{\rm B} T m^*}{eB\hbar}\right) = C - \frac{\pi m^*}{e\tau_{\rm SdH}} \frac{1}{B}$$
 (2)

where A is the amplitude of a resonance at field B and C is a constant. With the limited number of resonances observed, the measured value should be considered a rough estimate. From the plot of eq 2, the Dingle plot, we extrapolate a scattering time of 46 fs at 1.5 K, much longer than our graphene value of 1.4 fs. Together, the $50 \times$ longer scattering time combined with the $5 \times$ heavier effective mass is consistent with the order of magnitude increase in the mobility with the addition of PST.

Figure 3c shows the DFT band structure for the Gr/SnTe (111) interface. The graphene Dirac cone at Γ is gapped due to hybridization with SnTe. The highlighted bands (dashed lines) correspond to the 2DEG and originate from the top 2 layers of Sn and Te. Interestingly, these band structure calculations resemble the case of unpassivated SnTe³³ with the important difference being the graphene breaks the mirror symmetry, resulting in gaps of the Dirac cones and a loss of the topological state. The transport is thus dominated by the 2DEG that crosses the Fermi energy and is a result of the electronic redistribution to avoid the polar catastrophe. These band structure calculations show that conduction does not happen solely through the graphene layers but rather through this high mobility channel, consistent with experimental observations. This is even clearer when looking at the densities of states (DOS) shown in Figure 3d. The SnTe surface (solid blue line) dominates the DOS around the Fermi level with each atom contributing nearly 20× more states than either the graphene (dotted black line) or bulk SnTe (dashed red line).

At low field, a cusp can appear in the resistivity that is governed by the scattering mechanisms within the conduction channel. This could be weak localization (WL), commonly seen in graphene, or weak antilocalization (WAL), common in topological materials, the difference being whether the electrons interfere constructively or destructively. While there is no clear localization peak in the PST sample, suggesting the film is heavily doped into the conduction band, WL appears in both graphene and Gr/PST samples, as seen in Figure 2b. As we expect conduction to occur through the graphene due to a conductivity that is orders of magnitude higher than the PST, we model the cusp using the 2D WL model most often employed to analyze graphene, which accounts for spin—orbit, intervalley, and phase coherence scattering: 34-36

$$\Delta \sigma_{xx}(B) = -\frac{e^2}{2\pi h} \left[F\left(\frac{\tau_{\rm B}^{-1}}{\tau_{\phi}^{-1}}\right) - F\left(\frac{\tau_{\rm B}^{-1}}{\tau_{\phi}^{-1} + 2\tau_{i}^{-1}}\right) - 2F\left(\frac{\tau_{\rm B}^{-1}}{\tau_{\phi}^{-1} + \tau_{\rm SO}^{-1}}\right) \right]$$
(3)

where $F(x) = \ln(x) + \psi(1/2 + x^{-1})$ and with $\psi(x)$ being the digamma function. The parameter $\tau_B^{-1} = 4qD/\hbar B$, and τ_ϕ is the phase-coherence time. τ_i is the intervalley scattering time, and τ_{SO} is the spin-orbit scattering time. As is typical, the WL peak decreases as a function of temperature with the feature barely visible at 50 K and absent in the 100 K data, as shown in Figure 4a. We can combine these three scattering mechanisms to get a characteristic low field scattering time $\tau_{WL}^{-1} = \tau_i^{-1} + \tau_{\phi}^{-1} + \tau_{SO}^{-1}$, as shown in Figure 4b (red line). A temperature dependence of the constituent scattering times is shown in the inset.

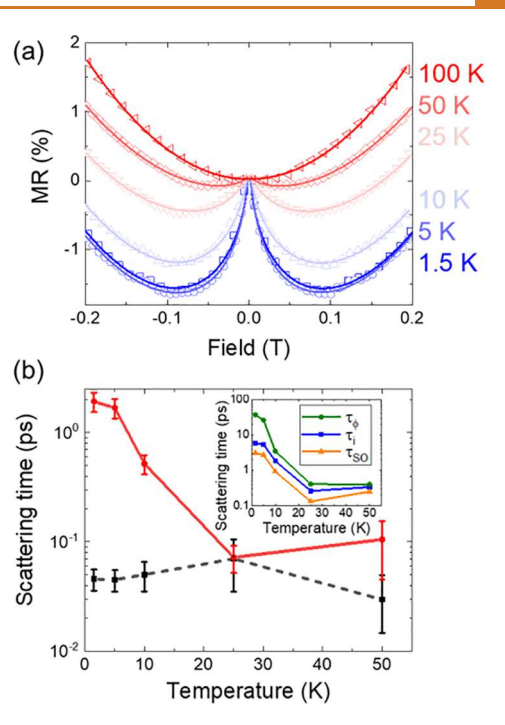


Figure 4. (a) Temperature dependence of the WL peak in Gr/PST. The WL cusp is completely suppressed by 100 K. The data (symbols) are given along with the associated fits to eq 3 (lines). (b) Characteristic scattering times for WL ($\tau_{\rm WL}$) and SdH ($\tau_{\rm SdH}$) regimes as a function of temperature. There is a clear transition in the WL scattering time around 25 K, suggesting a topological phase transition. (inset) Scattering times obtained as parameters from the WL fitting as a function of temperature. The scattering times in the (inset) are added in reciprocal to get the characteristic WL scattering time in (b).

We now want to compare τ_{WL} with the high-field scattering time obtained from the SdH oscillations, τ_{SdH} . Figure 4b shows both $\tau_{\rm SdH}$ and $\tau_{\rm WL}$ at temperatures up to 50 K. Above 25 K, the peaks become difficult to distinguish from the background, increasing the uncertainty (see Figure S5). Overall, $\tau_{\rm SdH}$ remains relatively constant around 50 fs, while $\tau_{\rm WL}$ shows a distinct transition around 25 K. One would expect the SdH momentum scattering time to be an average of the scattering times obtained from the WL fits ($\tau_{SO} = 1000 \text{ ps}, \tau_{\phi} = 7 \text{ ps}, \tau_{i} =$ 13 ps), as each mechanism in the WL model contributes to the momentum scattering events. This gives an estimate of the low-field scattering time of $\tau_{\rm WL} = 4.5$ ps, much longer than the high-field scattering time, $\tau_{\text{SdH}} = 0.046$ ps. This discrepancy in high- and low-field scattering times may be a result of spin splitting or field-induced asymmetry in the 2DEG bands. The magnetic field splits or skews the bands, altering the conduction paths and reducing the scattering time.

The 2DEG in Gr/PST is, however, analogous to the topologically protected surface states in topological insulators, like PST itself. In the case of topological materials, the surface states are protected by time reversal symmetry. Therefore, breaking time reversal symmetry, e.g., applying a magnetic field, destroys the topological state. ²⁶ In the case of Gr/PST, the 2DEG is protected by a special symmetry related to the polarization. The 2DEG could then be broken by defects or disorder that affects the polarization.

If we assume all scattering events are spin scattering events, the WL scattering time would be the spin scattering time. Therefore, we can use $\tau_{\text{WL}} = \tau_{\text{s}}$ as a lower bound on the spin

lifetime. Assuming a D'yakonov-Perel (DP) spin scattering mechanism, as has been observed in topological materials like Bi_2Se_3 as well as graphene with induced SOC, 34,37 we can approximate the strength of the spin—orbit interaction in our Gr/PST heterostructure. For the DP mechanism, spin relaxation occurs due to precession in a random effective magnetic field. In that case, the momentum (τ_q) and spin (τ_s) scattering times are related by the spin—orbit interaction strength Δ_{SO} according to

$$\tau_{\rm s}^{\rm DP} = \frac{h^2}{4\Delta_{\rm SO}^2 \tau_{\rm q}} \tag{4}$$

This yields an effective spin—orbit interaction of $\Delta_{SO}=1.2$ meV. This is significantly lower than the theoretical 33 meV interaction that can be induced in graphene by WS₂³⁸ but on par with experimental results in WS₂/graphene spin valves³⁴ and an order of magnitude larger than the 0.050 meV measured in suspended graphene devices.¹⁵

CONCLUSIONS

Magnetotransport provides an interesting picture of the interaction between graphene and PST with strong evidence of a charge redistribution to avoid the polar catastrophe. This heterostructure system manifests as a high mobility 2D conduction channel with 50 times longer scattering times compared to graphene. These properties suggest the Gr/PST heterostructure is an ideal candidate for further investigation, particularly as a spin transport channel. It also suggests that the polar catastrophe model could precipitate 2DEGs in other similar heterostructures created through stacking dissimilar materials. Further study of this system, both by theory and through DOS-probing techniques such as ARPES, could provide further insight into the interaction between topological and 2D materials. The improved mobility and scattering time suggest graphene/topological heterostructures could be utilized in a similar way as boron nitride encapsulation but with additional properties advantageous to computational device applications.

METHODS

Pb_{0.24}Sn_{0.76}Te (111) (PST) films were grown on GaAs (001) by MBE. Because the PST layers of interest are only 7 nm thick, we incorporated an electrically insulating chalcogenide-based buffer layer to decouple the interesting topological phenomenology of the PST from the unwanted effects of the GaAs substrate. Specifically, we used a sacrificial 10 nm Bi₂Se₃ starting layer, which adopts a (001) trigonal growth orientation upon which we grew a 20 nm (In,Bi)₂Se₃ followed by a 20 nm In₂Se₃ layer whose large trivial energy gap (1.3 eV) and smooth surface morphology make it a preferred surface for exploring the transport properties of the PST. The (001) trigonal symmetry of the sacrificial Bi₂Se₃ seeds the (111) orientation for the final PST layer of interest. Upon heating to >500 °C for an hour, all traces of Bi₂Se₃ completely evaporate, leaving the templated, atomically smooth In₂Se₃ upon which we use individual molecular beams of lead (Pb), tin (Sn), and tellurium (Te) to produce topological crystalline insulator (TCI) films having $Pb_{0.24}Sn_{0.76}Te$ composition. The stoichiometry is chosen to maximize the bulk band gap while maintaining the TCI behavior.³⁹ The PST (111) band structure is strongly dependent on surface passivation.³³ Previous modeling showed two well-isolated Dirac cones at Γ and M when the surface is passivated. However, for an unpassivated surface, the cones are not isolated and coexist with additional metallic energy bands. For our case, we assume that the bottom surface of the film is passivated by the substrate during MBE growth and the top surface is passivated

due to sustained exposure to the atmosphere. Likewise, the lack of observation of a strong electrically conducting state in bare PST corroborates these assumptions.

Films of PST were patterned into Hall bars using Shipley S1800 photoresist and optical lithography followed by etching in Ar/H₂ plasma. Another optical lithography step defined contacts, which were created with electron beam deposition of Ti/Au (5/50 nm) followed by lift-off in acetone. Graphene was grown by low-pressure (5–50 mTorr) chemical vapor deposition on copper foils at 1030 °C under flowing H₂ and CH₄ gas. ⁴⁰ After growth, the Cu foil substrates were etched and the remaining monolayer graphene films were transferred onto the predefined PST devices using a wet process (methods available elsewhere in the literature). ⁴¹ Another lithography step using poly(methyl methacrylate) (PMMA) and deep-UV photolithography was performed to again define the Hall bar mesas. PMMA and deep-UV lithography are used here to minimize chemical contamination of the graphene. ⁴² Excess graphene was subsequently removed with O₂ plasma.

The PST Hall bars were measured before and after the graphene transfer in order to directly compare changes in mobility and conductivity. Magnetotransport measurements were performed in a variable temperature He³ refrigerator equipped with a sample rotator within a 12 T superconducting magnet. We utilized a lock-in amplifier with independent preamplifiers and filters to simultaneously measure the longitudinal and transverse magnetoresistance. Results were consistent across 5 devices made from two nominally identical PST growths and processed at different times.

Raman spectra were measured in the backscattering arrangement. The sample was placed in a closed-cycle variable-temperature (5–300 K) cryostat. We used a Kr/Ar ion laser (488 to 647 nm) and a 532 nm diode laser as the laser sources. The laser power was limited to $<\!10~\rm kW/cm^2$ with 30 s exposure time to maximize the peak intensity and minimize the damage to the sample. An 1800-grooves/mm grating and a Si CCD were used to diffract and detect the scattered light, respectively.

We performed density-functional theory (DFT) calculations for structures similar to Gr/PST heterostructures to further explain the experimental results. Ab initio calculations were carried out using the projector-augmented wave method⁴³ as implemented in the Vienna ab initio simulation package (VASP).44 See the Supporting Information for further calculation details. Due to the size of the supercell needed to accurately describe alloyed PST, calculations are limited to two extreme cases: (i) a heterostructure formed of graphene on purely topological SnTe and (ii) heterostructures formed with the Sn atoms in the top N layers of SnTe replaced with Pb, denoted as NL-PbSnTe; e.g., 4L-PbSnTe has the top four layers of Sn replaced by Pb. The latter is equivalent to having N layers of the trivial insulator PbTe on top of the TI SnTe. Our calculations (see Figure S2) support that our alloyed $Pb_{0.24}Sn_{0.76}Te$ has the Sn and Pb species evenly distributed and lying somewhere between these two extremes on the topological side of the phase diagram.³⁹ In both cases, we look at the change in electronic structure with and without $(\sqrt{3} \times \sqrt{3})$ graphene on the (111) surface of the SnTe.

ASSOCIATED CONTENT

Supporting Information

The Supporting Information is available free of charge at https://pubs.acs.org/doi/10.1021/acsnano.2c08911.

As-measured Raman spectra, further calculations on Pb/Sn alloying, projected DOS for the bulk and surface atomic species, and information on SdH oscillation background subtraction as well as fits for the effective mass and scattering times (PDF)

AUTHOR INFORMATION

Corresponding Authors

Gregory M. Stephen — Laboratory for Physical Sciences,
College Park, Maryland 20740, United States; orcid.org/
0000-0002-8477-4438; Email: gstephen@lps.umd.edu
Adam L. Friedman — Laboratory for Physical Sciences, College
Park, Maryland 20740, United States; Email: afriedman@lps.umd.edu

Authors

Ivan Naumov — Howard University, Department of Physics and Astronomy, Washington, D.C. 20059, United States Nicholas A. Blumenschein — Laboratory for Physical Sciences, College Park, Maryland 20740, United States; orcid.org/0000-0002-6315-5734

Y.-J. Leo Sun — University of Maryland, Department of Electrical and Computer Engineering, College Park, Maryland 20742, United States

Jennifer E. DeMell – Laboratory for Physical Sciences, College Park, Maryland 20740, United States

Sharmila N. Shirodkar — Howard University, Department of Physics and Astronomy, Washington, D.C. 20059, United States; orcid.org/0000-0002-9040-5858

Pratibha Dev – Howard University, Department of Physics and Astronomy, Washington, D.C. 20059, United States

Patrick J. Taylor – US Army Research Laboratory, Adelphi, Maryland 20783, United States

Jeremy T. Robinson — US Naval Research Laboratory, Electronics Science and Technology Division, Washington, D.C. 20375, United States; ⊚ orcid.org/0000-0001-8702-2680

Paul M. Campbell – US Naval Research Laboratory, Electronics Science and Technology Division, Washington, D.C. 20375, United States

Aubrey T. Hanbicki — Laboratory for Physical Sciences, College Park, Maryland 20740, United States; orcid.org/ 0000-0001-8200-0378

Complete contact information is available at: https://pubs.acs.org/10.1021/acsnano.2c08911

Author Contributions

A.L.F. formulated the initial experimental idea. A.L.F. and G.M.S. designed the experiments with assistance from A.T.H. A.L.F fabricated the devices with assistance from P.M.C. J.T.R. grew and transferred graphene. P.J.T. grew the PST films. G.M.S. performed transport experiments and transport data analysis with assistance from J.E.D., N.A.B., P.M.C., A.T.H., and A.L.F. Raman spectroscopy, optical characterization, and analysis were performed by Y.-J.L.S. with assistance from J.T.R. and A.T.H. DFT modeling and analysis was performed by I.N., S.N.S., and P.D. G.M.S., A.T.H., I.N., and A.L.F. wrote the manuscript. All authors contributed to discussions of the results and editing the manuscript.

Notes

The authors declare no competing financial interest.

ACKNOWLEDGMENTS

The authors from LPS gratefully acknowledge critical assistance from the LPS support staff including G. Latini, J. Wood, R. Brun, P. Davis, and D. Crouse. The authors from LPS and ARL along with P.M.C. gratefully acknowledge support from the Applied Research for the Advancement of

S&T Priorities program of the Office of the Secretary of Defense. Work at NRL was supported by the Office of Naval Research through Base programs at NRL. P.D., I.N., and S.N.S. acknowledge support by the W. M. Keck Foundation and the NSF Grant number DMR-1752840. The computational resources were provided by the Extreme Science and Engineering Discovery Environment (XSEDE) under Project PHY180014, which was supported by the National Science Foundation grant number ACI-1548562.

REFERENCES

- (1) Warusawithana, M. P.; Richter, C.; Mundy, J. A.; Roy, P.; Ludwig, J.; Paetel, S.; Heeg, T.; Pawlicki, A. A.; Kourkoutis, L. F.; Zheng, M.; Lee, M.; Mulcahy, B.; Zander, W.; Zhu, Y.; Schubert, J.; Eckstein, J. N.; Muller, D. A.; Hellberg, C. S.; Mannhart, J.; Schlom, D. G. LaAlO₃ Stoichiometry Is Key to Electron Liquid Formation at LaAlO₃/SrTiO₃ Interfaces. *Nat. Commun.* **2013**, *4* (1), 2351.
- (2) Stengel, M. First-Principles Modeling of Electrostatically Doped Perovskite Systems. *Phys. Rev. Lett.* **2011**, *106* (13), 136803.
- (3) Naumov, I. I.; Hemley, R. J. Metallic Surface States in Elemental Electrides. *Phys. Rev. B* **2017**, *96* (3), 035421.
- (4) Stemmer, S.; Allen, S. J. Two-Dimensional Electron Gases at Complex Oxide Interfaces. *Annu. Rev. Mater. Res.* **2014**, 44 (1), 151–171
- (5) Gibney, E. Nobel for Blue LED That Revolutionized Lighting. *Nature* **2014**, *514* (7521), 152–153.
- (6) Ebert, G.; von Klitzing, K.; Maan, J. C.; Remenyi, G.; Probst, C.; Weimann, G.; Schlapp, W. Fractional Quantum Hall Effect at Filling Factors up to N=3. *Journal of Physics C: Solid State Physics* 1984, 17 (29), L775–L779.
- (7) Liu, Y.; Huang, Y.; Duan, X. Van Der Waals Integration before and beyond Two-Dimensional Materials. *Nature* **2019**, *567* (7748), 323–333
- (8) Liu, Y.; Weiss, N. O.; Duan, X.; Cheng, H.-C.; Huang, Y.; Duan, X. Van Der Waals Heterostructures and Devices. *Nat. Rev. Mater.* **2016**, *1* (9), 16042.
- (9) Hasan, M. Z.; Kane, C. L. Colloquium: Topological Insulators. *Rev. Mod. Phys.* **2010**, 82 (4), 3045–3067.
- (10) Jafarpisheh, S.; Cummings, A. W.; Watanabe, K.; Taniguchi, T.; Beschoten, B.; Stampfer, C. Proximity-Induced Spin-Orbit Coupling in Graphene/Bi_{1.5}Sb_{0.5}Te_{1.7}Se_{1.3} Heterostructures. *Phys. Rev. B* **2018**, 98 (24), 241402.
- (11) Friedman, A. L.; Hanbicki, A. T.Prolegomena To Any Future Device Physics. *arXiv* (Physics and Society), October 29, 2021, 2110.15822, Ver 1; https://arxiv.org/abs/2110.15822.
- (12) Lau, Y. C.; Betto, D.; Rode, K.; Coey, J. M. D.; Stamenov, P. Spin-Orbit Torque Switching without an External Field Using Interlayer Exchange Coupling. *Nat. Nanotechnol.* **2016**, *11* (9), 758–762.
- (13) Lu, J. W.; Chen, E.; Kabir, M.; Stan, M. R.; Wolf, S. A. Spintronics Technology: Past, Present and Future. *International Materials Reviews* **2016**, *61* (7), 456–472.
- (14) Manipatruni, S.; Nikonov, D. E.; Lin, C.-C.; Gosavi, T. A.; Liu, H.; Prasad, B.; Huang, Y.-L.; Bonturim, E.; Ramesh, R.; Young, I. A. Scalable Energy-Efficient Magnetoelectric Spin—Orbit Logic. *Nature* **2019**, *565* (7737), 35–42.
- (15) Guimarães, M. H. D.; Veligura, A.; Zomer, P. J.; Maassen, T.; Vera-Marun, I. J.; Tombros, N.; van Wees, B. J. Spin Transport in High-Quality Suspended Graphene Devices. *Nano Lett.* **2012**, *12* (7), 3512–3517.
- (16) Sverdlov, V.; Selberherr, S. Silicon Spintronics: Progress and Challenges. *Phys. Rep.* **2015**, 585, 1–40.
- (17) Han, W.; Kawakami, R. K.; Gmitra, M.; Fabian, J. Graphene Spintronics. *Nat. Nanotechnol.* **2014**, *9* (10), 794–807.
- (18) Zollner, K.; Fabian, J. Single and Bilayer Graphene on the Topological Insulator Bi₂Se₃: Electronic and Spin-Orbit Properties from First Principles. *Phys. Rev. B* **2019**, *100* (16), 165141.

- (19) Wiendlocha, B. Resonant Levels, Vacancies, and Doping in Bi₂Te₃, Bi₂Te₂Se, and Bi₂Se₃ Tetradymites. J. Electron. Mater. **2016**, 45 (7), 3515-3531.
- (20) Stephen, G. M.; Naumov, I.; Tyagi, S.; Vail, O. A.; DeMell, J. E.; Dreyer, M.; Butera, R. E.; Hanbicki, A. T.; Taylor, P. J.; Mayergoyz, I.; Dev, P.; Friedman, A. L. Effect of Sn Doping on Surface States of Bi₂Se₃ Thin Films. J. Phys. Chem. C 2020, 124 (49), 27082-27088.
- (21) Ohtomo, A.; Hwang, H. Y. A High-Mobility Electron Gas at the LaAlO₃/SrTiO₃ Heterointerface. Nature 2004, 427 (6973), 423-426.
- (22) Casiraghi, C.; Pisana, S.; Novoselov, K. S.; Geim, A. K.; Ferrari, A. C. Raman Fingerprint of Charged Impurities in Graphene. Appl. Phys. Lett. 2007, 91 (23), 233108.
- (23) Mohiuddin, T. M. G.; Lombardo, A.; Nair, R. R.; Bonetti, A.; Savini, G.; Jalil, R.; Bonini, N.; Basko, D. M.; Galiotis, C.; Marzari, N.; Novoselov, K. S.; Geim, A. K.; Ferrari, A. C. Uniaxial Strain in Graphene by Raman Spectroscopy: G Peak Splitting, Grüneisen Parameters, and Sample Orientation. Phys. Rev. B 2009, 79 (20),
- (24) Hsieh, T. H.; Lin, H.; Liu, J.; Duan, W.; Bansil, A.; Fu, L. Topological Crystalline Insulators in the SnTe Material Class. Nat. Commun. 2012, 3 (1), 982.
- (25) Taherinejad, M.; Garrity, K. F.; Vanderbilt, D. Wannier Center Sheets in Topological Insulators. Phys. Rev. B 2014, 89 (11), 115102.
- (26) Bristowe, N. C.; Ghosez, P.; Littlewood, P. B.; Artacho, E. The Origin of Two-Dimensional Electron Gases at Oxide Interfaces: Insights from Theory. J. Phys.: Condens. Matter 2014, 26 (14), 143201.
- (27) Kretinin, A. V.; Cao, Y.; Tu, J. S.; Yu, G. L.; Jalil, R.; Novoselov, K. S.; Haigh, S. J.; Gholinia, A.; Mishchenko, A.; Lozada, M.; Georgiou, T.; Woods, C. R.; Withers, F.; Blake, P.; Eda, G.; Wirsig, A.; Hucho, C.; Watanabe, K.; Taniguchi, T.; Geim, A. K.; Gorbachev, R. V. Electronic Properties of Graphene Encapsulated with Different Two-Dimensional Atomic Crystals. Nano Lett. 2014, 14 (6), 3270-3276.
- (28) Singh, S.; Gopal, R. K.; Sarkar, J.; Pandey, A.; Patel, B. G.; Mitra, C. Linear Magnetoresistance and Surface to Bulk Coupling in Topological Insulator Thin Films. J. Phys.: Condens. Matter 2017, 29 (50), 505601.
- (29) Assaf, B. A.; Cardinal, T.; Wei, P.; Katmis, F.; Moodera, J. S.; Heiman, D. Linear Magnetoresistance in Topological Insulator Thin Films: Quantum Phase Coherence Effects at High Temperatures. Appl. Phys. Lett. 2013, 102 (1), 012102.
- (30) Ashcroft, N. W.; Mermin, N. D.Solid State Physics; Saunders College: Belmont, 1976.
- (31) Heinzel, T.Magneto-Transport Properties of Quantum Films. In Mesoscopic Electronics in Solid State Nanostructures; Wiley-VCH: Darmstadt, 2006; pp 147-176; DOI: 10.1002/9783527618910.ch6.
- (32) Avsar, A.; Tan, J. Y.; Taychatanapat, T.; Balakrishnan, J.; Koon, G. K. W.; Yeo, Y.; Lahiri, J.; Carvalho, A.; Rodin, A. S.; O'Farrell, E. C. T.; Eda, G.; Neto, A. H. C.; Özyilmaz, B. Spin-Orbit Proximity Effect in Graphene. Nat. Commun. 2014, 5 (1), 4875.
- (33) Shi, Y.; Wu, M.; Zhang, F.; Feng, J. 111) Surface States of SnTe. Phys. Rev. B 2014, 90 (23), 235114.
- (34) Friedman, A. L.; McCreary, K. M.; Robinson, J. T.; van't Erve, O. M. J.; Jonker, B. T. Spin Relaxation and Proximity Effect in WS₂/ Graphene/Fluorographene Non-Local Spin Valves. Carbon 2018, 131, 18-25.
- (35) Hikami, S.; Larkin, A. I.; Nagaoka, Y. Spin-Orbit Interaction and Magnetoresistance in the Two Dimensional Random System. Prog. Theor. Phys. 1980, 63 (2), 707-710.
- (36) Friedman, A. L.; Cress, C. D.; Schmucker, S. W.; Robinson, J. T.; van't Erve, O. M. J. Electronic Transport and Localization in Nitrogen-Doped Graphene Devices Using Hyperthermal Ion Implantation. Phys. Rev. B 2016, 93 (16), 161409.
- (37) Sun, R.; Yang, S.; Yang, X.; Kumar, A.; Vetter, E.; Xue, W.; Li, Y.; Li, N.; Li, Y.; Zhang, S.; Ge, B.; Zhang, X.; He, W.; Kemper, A. F.; Sun, D.; Cheng, Z. Visualizing Tailored Spin Phenomena in a

- Reduced-Dimensional Topological Superlattice. Adv. Mater. 2020, 32 (49), 2005315.
- (38) Kaloni, T. P.; Kou, L.; Frauenheim, T.; Schwingenschlögl, U. Quantum Spin Hall States in Graphene Interacting with WS2 or WSe₂. Appl. Phys. Lett. **2014**, 105 (23), 233112.
- (39) Xu, S.-Y.; Liu, C.; Alidoust, N.; Neupane, M.; Qian, D.; Belopolski, I.; Denlinger, J. D.; Wang, Y. J.; Lin, H.; Wray, L. A.; Landolt, G.; Slomski, B.; Dil, J. H.; Marcinkova, A.; Morosan, E.; Gibson, Q.; Sankar, R.; Chou, F. C.; Cava, R. J.; Bansil, A.; Hasan, M. Z. Observation of a Topological Crystalline Insulator Phase and Topological Phase Transition in Pb_{1-x}Sn_xTe. Nat. Commun. 2012, 3 (1), 1192.
- (40) Li, X.; Magnuson, C. W.; Venugopal, A.; Tromp, R. M.; Hannon, J. B.; Vogel, E. M.; Colombo, L.; Ruoff, R. S. Large-Area Graphene Single Crystals Grown by Low-Pressure Chemical Vapor Deposition of Methane on Copper. J. Am. Chem. Soc. 2011, 133 (9), 2816-2819.
- (41) Robinson, J. T.; Schmucker, S. W.; Diaconescu, C. B.; Long, J. P.; Culbertson, J. C.; Ohta, T.; Friedman, A. L.; Beechem, T. E. Electronic Hybridization of Large-Area Stacked Graphene Films. ACS *Nano* **2013**, 7 (1), 637–644.
- (42) Arnold, H. N.; Sangwan, V. K.; Schmucker, S. W.; Cress, C. D.; Luck, K. A.; Friedman, A. L.; Robinson, J. T.; Marks, T. J.; Hersam, M. C. Reducing Flicker Noise in Chemical Vapor Deposition Graphene Field-Effect Transistors. Appl. Phys. Lett. 2016, 108 (7),
- (43) Kresse, G.; Joubert, D. From Ultrasoft Pseudopotentials to the Projector Augmented-Wave Method. Phys. Rev. B 1999, 59 (3), 1758 - 1775.
- (44) Kresse, G.; Furthmüller, J. Efficient Iterative Schemes for Ab Initio Total-Energy Calculations Using a Plane-Wave Basis Set. Phys. Rev. B 1996, 54 (16), 11169-11186.

□ Recommended by ACS

Addressing Electron Spins Embedded in Metallic Graphene **Nanoribbons**

Niklas Friedrich, José Ignacio Pascual, et al.

AUGUST 29, 2022

ACS NANO

READ 2

Defect-Density- and Rashba-Shift-Induced Interfacial Dzyaloshinskii-Moriya Interaction and Spin Pumping in Single-Layer Graphene/Co₂₀Fe₆₀B₂₀ Heterostructures:...

Amrit Kumar Mondal, Anjan Barman, et al.

MARCH 21, 2022

ACS APPLIED NANO MATERIALS

READ

All-Electrical Spin-to-Charge Conversion in Sputtered Bi, Se,

Won Young Choi, Fèlix Casanova, et al.

SEPTEMBER 26, 2022

NANO I ETTERS

READ **Z**

Graphene Lattices with Embedded Transition-Metal Atoms and Tunable Magnetic Anisotropy Energy: Implications for **Spintronic Devices**

Rostislav Langer, Piotr Błoński, et al.

JANUARY 18, 2022

ACS APPLIED NANO MATERIALS

READ

Get More Suggestions >